An efficient level-set flame propagation model for hybrid unstructured grids using the G-Equation

Federico Perini[a], Youngchul Ra[b]
Kenji Hiraoka[c], Kazutoshi Nomura[c], Akihiro Yuuki[c], Yuji Oda[c]
Christopher J. Rutland[a], Rolf D. Reitz[a]

[a]University of Wisconsin-Madison
[b]Michigan Technological University
[c]Mitsubishi Heavy Industries, ltd.

Abstract

Computational fluid dynamics of gas-fueled large-bore spark ignition engines with pre-chamber ignition can speed up the design process of these engines provided that 1) the reliability of the results is not affected by poor meshing and 2) the time cost of the meshing process does not negatively compensate for the advantages of running a computer simulation. In this work a flame propagation model that runs with arbitrary hybrid meshes was developed and coupled with the KIVA4-MHI CFD solver, in order to address these aims. The solver follows the G-Equation level-set method for turbulent flame propagation by Tan and Reitz, and employs improved numerics to handle meshes featuring different cell types such as hexahedra, tetrahedra, square pyramids and triangular prisms.

Detailed reaction kinetics from the SpeedCHEM solver are used to compute the non-equilibrium composition evolution downstream and upstream of the flame surface, where chemical equilibrium is instead assumed. A generalized least-squares gradient reconstruction algorithm is employed to evaluate spatial derivatives with arbitrary node and cell connectivities, instead of the original ENO scheme. Finally, a new, extended version of the “marching cubes” algorithm for iso-surface tracking was developed and implemented for all four employed cell types.

The solver was tested across different cell types and cell resolutions by simulating spherical ignition in a simple cylindrical combustion chamber. Validation was performed against experimental measurements of torch jet ignition with a diaphragm and of pre-chamber gaseous fuel combustion two-chamber experimental vessel separated by a variable-diameter nozzle, with different grid resolutions.

Introduction

The success of advanced, fuel-efficient and environmentally friendly combustion strategies for internal combustion engines is challenged by the need to meet increasingly stringent regulatory emission mandates [1]. Multi-dimensional Computational Fluid Dynamics (CFD) simulations have become a mandatory design tool for the exploration and implementation of high-efficiency, lean combustion regimes also for gas-fueled spark ignition engines, thanks to recent advancements in:

- in-cylinder flow and turbulence modeling, through large-eddy simulations (LES) [2] for capturing most eddy scales and their effects on cycle-to-cycle variations; and anisotropic models for Reynolds-Averaged Navier Stokes simulations (RANS) [3,4];
- methods for chemical kinetics modeling of hydrocarbon ignition processes [5,6], and their application to premixed and partially-premixed combustion [7,8];
- sub-grid scale gas jet injection modeling for practical engine grid sizes [9-11];
- flame propagation and flame-wall interaction modeling for RANS and LES engine simulations [12-15].

Natural-gas-fueled engines are naturally attractive for heavy duty applications because of the cheap fuel cost and cheaper pollutant control devices allowed by globally lean engine operation; as well as for significantly lower greenhouse-gas emission, which can be as much as 25% smaller than from traditional heavy hydrocarbon fuels. Lean combustion strategies are an effective way to reduce NOx emissions and to increase the overall thermodynamic efficiency by reducing wall heat losses, but they must be carefully designed to avoid reaching the lower natural gas’s ignitability limit.

In order to cope with this issue, among other charge ignition strategies such as with a pilot injection of diesel or of a secondary, high-reactivity fuel [16,17], pre-chamber-type devices have been proposed, and studied in a variety of configurations [18-21]. By using a pre-chamber, a near-stoichiometric or slightly rich mixture can be formed and ignited upstream of the combustion chamber in an almost-closed volume. The ignited charge then propagates into the combustion chamber by forming torch-shaped jets, that azimuthally cover the whole combustion chamber and ignite its lean air-fuel mixture, as schematically reported in Figure 1.

Computational modeling of such an engine configuration is challenging. The pre-chamber simulation cannot be decoupled from the combustion chamber simulation. In case a block-structured hexahedral grid is used, a unique complex blocking structure must be defined, and the mesh needs to be basically re-made each time a new pre-chamber geometry is to be tested. Second, the time and spatial scales in the pre-chamber do not allow proper resolution of the flame front development and its near-sound-speed travel within the pre-chamber nozzles. For the purpose of modeling heavy-duty gas-fueled

pre-chamber ignition engines, it is necessary to develop a methodology that:

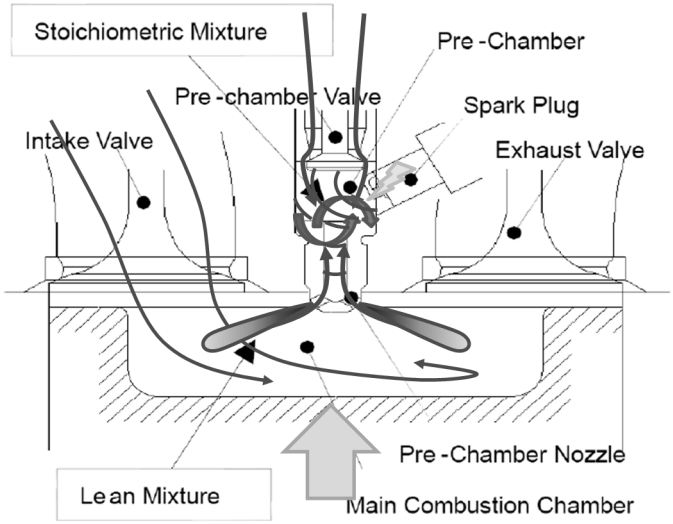

Figure 1. Pre-chamber mixture formation and ignition schematic.

1) features hybrid unstructured body-fitted grids, so that multiple pre-chamber meshes can be generated using automated meshing techniques, without compromising for simulation accuracy near the walls or in narrow regions such as the nozzles;
2) incorporates detailed chemical kinetics for the accurate prediction of the flame front advancement at the lean limit, as well as accurate pollutant formation from the combustion products;
3) tracks all relevant flame propagation properties at mesh scales of typical combustor geometries, hence without having to discretize the inner- and near-inner-flame structure.

In this work we present the development of a computationally efficient methodology suitable for the design of pre-chamber ignition heavy-duty gas-fueled engines. The methodology features an enhanced level-set turbulent flame propagation model using the G-Equation [12]. A new 'marching cells' algorithm, or an extended iso-surface and iso-volume tracking method for hybrid unstructured grids was developed. The methodology was embedded in an Arbitrary Lagrangian-Eulerian finite volume scheme [22]. Consistency and accuracy of the flame propagation scheme were assessed across meshes featuring different cell types, and validated versus experimental optical measurements of torch-jet flame propagation in restricted channels, representative of pre-chamber-like operation.

Flame Propagation Model Description

Flame propagation in spark-ignited premixed and partially-premixed combustion regimes follows time and spatial scales which cannot be typically captured with the finite volume method on devices of industrial scale such as internal combustion engines.

The laminar flame structure is typically represented as three adjacent layers, for an overall thickness l_F which can be estimated as [12]

$$l_F = \frac{\lambda / c_p\big|_{T=T_0}}{\rho_u S_{L0}}. \quad (1)$$

The bulk of the flame thickness is occupied by an inert pre-heating region where temperature rises but no significant reactions occur. An inner reactive-diffusive layer δ (Figure 2) is a thin portion of the whole thickness, where the fuel is consumed and chemical reactions occur in a diffusion-limited process. A final, slightly thicker oxidation layer, ε, relevant to CO production, is reported to be approximately three times larger, $\varepsilon \, l_F \sim 3\delta \, l_F$.

As summarized for example by the flamelet modeling theory of Peters [23] – and using the nomenclature reported in Figure 2 –, turbulent flame propagation in engines happens under either the corrugated flamelet regime, where the whole flame reaction-diffusion region is embedded within eddies at the Kolmogorov scale; or the thin-reaction-zone regime, which assumes that Kolmogorov eddies can enter the inert zone ahead of the reactive-diffusive region, but not the inner flame layer where the chemical reactions take place.

Peters demonstrated that the inner flame structure is either undisturbed by the smallest eddies (corrugated flamelet), or it can be tracked via an augmented displacement speed and diffusion coefficient (thin-reaction-zone), which incorporate the effects of strain. It is hence possible to describe transport of the flame inner layer using the same equation valid for both regimes.

The inner flame layer is hence modeled as a two-dimensional, faceted interface of infinitesimal thickness, which is ruled by a transport equation.

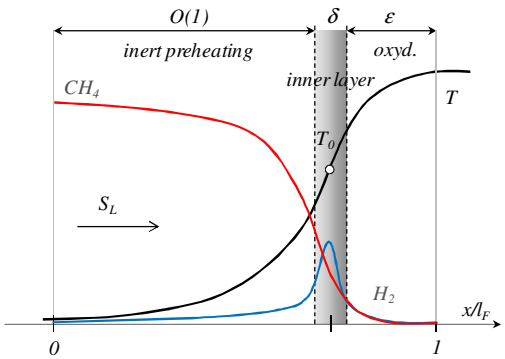

Figure 2. Schematic of asymptotic one-dimensional laminar flamelet structure for a methane-air flame (re-made from [23]) versus normalized flame thickness coordinate x/l_F.

G-Equation level-set Flame Formulation

The "G-Equation model" is a flamelet model using the level set method for the solution of the flame front transport equation first proposed by Peters [12]. Level set modeling is a class of tools for handling surface treatment in multi-dimensional models, where the surface is tracked using a level set from a multi-dimensional scalar field (such as the iso-surface **G** = 0) [24]. The current study builds on the G-Equation formulation first developed by Fan and Reitz [25], and later improved by Tan and Reitz [14] and Liang and Reitz [7].

In the G-Equation, a transport equation describing the dynamics of the G = 0 flame front is used:

$$\rho\frac{DG}{Dt}=\rho\frac{\partial G}{\partial t}+\rho\mathbf{u}\cdot\nabla G=\left(\rho S_L^0\right)\sigma-\left(\rho D\right)\kappa\sigma, \qquad (2)$$

where σ is a turbulent to laminar flame surface area or flame speed ratio, expressed as:

$$\sigma=\frac{S_T^0}{S_L^0}=1+\frac{S_T^0-S_L^0}{S_L^0}=\left|\nabla G\right|+\sigma_T, \qquad (3)$$

σ_T being a turbulent contribution term. Within the Reynolds-Averaged Navier Stokes flow representation and k-ε turbulence modeling approach, Equation (2) can be expressed as a Favre-averaged G field (no superscript), plus a variance field (tilde superscript) equation that serves the computation of the σ_T term:

$$\begin{cases}\dfrac{\partial G}{\partial t}+\mathbf{u}\cdot\nabla G=\dfrac{\rho_u}{\rho}S_T^0\left|\nabla G\right|-D_T\kappa\left|\nabla G\right|,\\ \dfrac{\partial\tilde{G}}{\partial t}+\mathbf{u}\cdot\nabla\tilde{G}=\nabla_{\|}\cdot\left(\dfrac{\rho_u}{\rho}D_T\nabla_{\|}\tilde{G}\right)+2D_T\left(\nabla\tilde{G}\right)^2-c_s\dfrac{\tilde{\varepsilon}}{\tilde{k}}\tilde{G},\end{cases} \qquad (4)$$

where $\nabla_{||}$ indicates a tangential gradient operator, **u** the Favre-averaged fluid velocity, ρ_u and ρ the density of unburnt and burnt flamelet sides, D_T the turbulent diffusivity, c_s a modeling constant, and:

$$\kappa=\nabla\cdot\left(\frac{\nabla G}{\left|\nabla G\right|}\right) \qquad (5)$$

the Favre-averaged flame front curvature.

Ignition Kernel Modeling

Even with a level set approach a tiny spherical flame front of size less than the mesh during ignition kernel development cannot be resolved by the G-Equation. Hence, the Discrete Particle Ignition Kernel (DPIK) model of Tan and Reitz [14] was implemented and employed.

In this model, the flame front during kernel growth is tracked using Lagrangian particle tracers instead of the G-field solution, and the flame surface density is computed as the number density of particles in each finite volume cell. The ignition kernel is assumed to be perfectly spherical and internally homogeneous (ρ_k), and a time law for the rate of change of kernel radius is used:

$$\frac{dr_k}{dt}=\frac{\rho_u}{\rho_k}\left(S_{plasma}+S_T\right), \qquad (6)$$

where the plasma velocity is based on an energy balance of the ignition kernel as a closed thermodynamic system:

$$S_{plasma}=\frac{\eta_{el}\dot{Q}_{el}}{4\pi r_k^2\left[\rho_u\left(u_k-h_u\right)+p\dfrac{\rho_u}{\rho_k}\right]}. \qquad (7)$$

Q_{el} represents non-ideal power transfer to the fluid due to the spark discharge, subject to an efficiency $\eta_{el} = 0.3$, *p, u* and *h* are pressure, internal energy and enthalpy and the *u* subscript represents the unburnt region outside of the kernel. The turbulent flame speed term S_T contains a flame stretch factor according to Herweg *et al.* [36]:

$$S_T=S_L^0\left[1-\left(\frac{l_F}{15l_I}\right)^{\frac{1}{2}}\left(\frac{u'}{S_L^0}\right)^{\frac{3}{2}}-2\frac{l_F}{r_k}\frac{\rho_u}{\rho_k}\right], \qquad (8)$$

where l_I is the integral turbulence length scale. The transition from the DPIK model to the G-Equation solver is based on a critical radius criterion:

$$r_k\geq c_{m1}l_I=c_{m1}\,0.16\frac{k^{3/2}}{\varepsilon}, \qquad (10)$$

where c_{m1} is a model constant usually greater than unity [14].

Currently, transition to the G-Equation solver can only be initiated by the ignition kernel model. Auto-ignition (especially knock-related) phenomena are predicted via the detailed chemistry integration (cf. next paragraph), but are not allowed to initiate a new flame front. Future research will need to focus on incorporating a Borghi-diagram-based condition to define when ignition chemistry should switch to flame propagation (for both premixed and non-premixed combustion regimes).

Detailed Chemical Kinetics-based Combustion Modeling

The availability of detailed chemical kinetic mechanisms for the oxidation of hydrocarbons has had a major impact on the accuracy of internal combustion engine simulations, because of:

1) the ability to characterize ignition delay, combustion development and heat release at a variety of

thermodynamic combustion regimes with a same reaction model, which would be unfeasible with simplified ignition schemes;

2) a physics-based pollutant formation description through usage of their direct gas-phase components (NOx, UHC) or precursors (soot);
3) a more accurate description of the local presence of highly-reactive radicals in the multi-dimensional domain, whose transport equations are solved for by the flow solver.

However, its application to multidimensional internal combustion engine simulations is still limited because of the extreme computational burden required to solve the stiff systems of ordinary differential equations (ODEs) associated with reactive networks often featuring hundreds/thousands of species and reactions.

In the present work, detailed combustion kinetics using the SpeedCHEM sparse analytical Jacobian chemistry solver [5,6] were coupled with the G-Equation solver.

Non-flame cells. In the model direct chemistry integration is employed to compute the rates of change of species mass fractions due to chemical reactions, treating each computational cell as a homogeneous well-stirred reactor. The reaction mechanism describes a set of n_r reactions among n_s species:

$$\sum_{i=1}^{n_s} \nu'_{k,i} M'_i \leftrightarrow \sum_{i=1}^{n_s} \nu''_{k,i} M''_i, \qquad k = 1,\ldots,n_r, \tag{11}$$

with ν' and ν'' being stoichiometric reactant/product reaction coefficients, and M the species names. The temporal evolution of the thermodynamic state of the reacting gas-phase mixture with species mass conservation is described by:

$$\frac{dY_i}{dt} = \frac{W_i}{\rho} \sum_{k=1}^{n_r} \left(\nu''_{k,i} - \nu'_{k,i}\right) q_k, \quad i = 1,\ldots,n_s, \tag{12}$$

with q_k the reaction rate progress variables, W the species molecular weights, and ρ the mixture density. The mass conservation constraint: $\Sigma Y_i = 1$, or $\Sigma dY_i/dt = 0$, is automatically verified if the reactions are well-posed, i.e., each one verifies atomic conservation of all chemical elements. In the multi-dimensional domain, the energy conservation resembles a temperature rate of change in an adiabatic constant-volume reactor:

$$\frac{dT}{dt} = -\frac{1}{\bar{c}_v} \sum_{i=1}^{n_s} \left(\frac{U_i}{W_i} \frac{dY_i}{dt} \right), \tag{13}$$

U being molar internal energies, $\bar{c}_v$ the mixture average specific heat at constant volume in mass units.

The code also features libraries for the evaluation of thermodynamic properties of gas-phase mixtures and kinetic laws for various reaction classes (Arrhenius, three-body, reversible/irreversible, mapped pressure-dependent, etc.). All of the equations employ a matrix-based representation that makes use of an object-oriented sparse matrix algebra library, specifically developed for this application. A sparse analytical Jacobian matrix formulation was developed to speed up the most demanding parts of the integration of the ODE system [5].

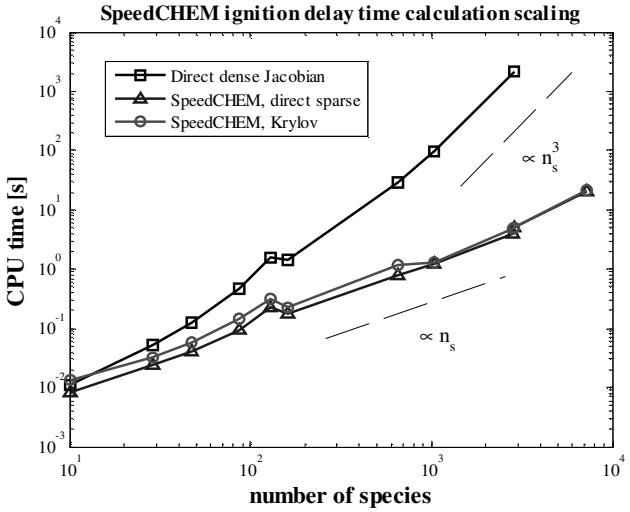

Figure 3 - Linear scalability of the SpeedCHEM solver for constant-volume well stirred reactor calculations. (black) dense, (blue) sparse, (red) Krylov linear system solver comparison. Adapted from [6].

Coupled with a variety of stiff ODE solvers, the SpeedCHEM package has been demonstrated to achieve up to three orders of magnitude speed up in comparison with the dense CHEMKIN-II library, showing order-of-magnitude speedups also for small reaction mechanisms typically used in large multi-dimensional simulations, as reported in Figure 3. The constant-volume reactor calculation in all non-flame cells also provides a good estimate of whether knock will occur in the end gases [8].

Flame cells. In cells containing the flame front, the method of Liang was applied [7]. Where a flame front is present (with total area A_f), two – not necessarily unique and contiguous – volumes can be geometrically identified within the cell: an unburnt mixture volume V_u and a burnt volume V_b containing combustion products.

The volume containing combustion products, and swept by the flame front, is assumed to be in local equilibrium at the homogeneous cell pressure (deflagration behavior). Its mass fraction composition $Y_{i,b}$ is computed using an equilibrium calculation code [27], which also provides an adiabatic flame temperature that is assumed to be constant across the burnt volume region, $T_{equil} = T_b$. The burnt gas species and mixture densities are given directly from the equation-of-state.

The unburnt species densities can be estimated based on simple mass conservation of the unburnt volume, which is swept by the flame surface. The exact swept volume is evaluated as the difference between the burnt volumes in the

cell, computed using the flame triangulation, before (time 'n') and after (phase 'B') the G field advancement. The global rate of species density change can hence be evaluated as:

$$\frac{\partial \rho_i}{\partial t} = \left(\rho Y_{i,b} - \rho_i\right)\frac{V_b^B - V_b^n}{V_u}, \quad i = 1,..., n_s . \tag{14}$$

No special treatment is applied in case the flame front reaches cells which contain mostly combustion products on its 'unburnt' side. In this unlikely event, when swept by the flame front, they will eventually experience 1) a slow flame speed, because of the extremely low value of ϕ; 2) a limited species conversion rate and corresponding heat release, as the 'unburnt' composition ahead of the flame front contains gases which are already close to their corresponding equilibrium composition.

Flame speed. Laminar flame speed calculations with detailed chemical kinetics require a one-dimensional representation of the laminar flame, which is usually discretized using a finite-difference approach. Fixed point algorithms are needed to solve the coupled nonlinear reaction-diffusion flame equations (also including nonlinear binary diffusion coefficients for each species pair). Even using sparse algebra, this type of calculation requires a CPU time which is of the order of minutes for a single laminar flame configuration, making its adoption practically unfeasible on a large multidimensional domain. While a tabulation approach could be used, it would require to compromise on the species composition on both sides (burnt/unburnt). Also, its accuracy could deteriorate in full-cycle engine calculations where a wide range of pressures is swept. Hence, we decided to adopt mapped laminar flame speed correlations which were verified to be adequate at the pressure ranges experienced by the simulation, and that feature similar input (T, phi, p) as a table would have. Still, this remains a challenging topic and potential improvement for future research.

Table 1. Details of Marching Cells iso-surface configurations.

Cell Type	edges	nodes	faces	cfg #
Hexahedron	12	8	6	256
Flatiron	9	6	5	64
Pyramid	8	5	5	32
Tetrahedron	6	4	4	16

Numerical Solution Method

The G-Equation level set representation of the flame front has physical meaning only at the flame front itself, or at the iso-surface defined by **G** = *0*. Hence, in our implementation, the G-Equation is solved only at set of flame 'brush' nodes, identified as the ones belonging to cells which contain the flame front; a dummy value of G equal to the signed distance from the flame is instead used far away from the flame.

As the accuracy of the flame equation solution relies on proper calculation of the field gradient and curvature at the flame front, a methodology for iso-surface tracking and handling via a discretized triangulation, and a numerical scheme for spatial derivative evaluation on general unstructured grids are proposed in this study.

A 'Marching Cells' algorithm for iso-surface triangulation

The 'Marching Cubes' algorithm proposed by Lorensen and Cline [28] is the first of a family of the currently most widely adopted surface-reconstruction methods from three-dimensional data [29,30].

While this algorithm is mainly employed in computer graphics post-processors, it was chosen as a basis for our methodology for the following reasons:

- a non-ambiguous iso-surface triangulation is determined by processing each hexahedron independently (hence the name 'marching cubes'). This makes the algorithm intrinsically fast because it is fully vectorizable;
- all triangulation vertices are uniquely identified at the cell's edges, which makes the methodology 1) easily extensible to hybrid meshes with cells of any kind, and 2) fast as each flame edge, which is shared by several cells, is only processed once;
- the edge piercing point identification principle is based on a multi-linear field interpolation which follows a parameterized representation of the cell. The same parameterization can be exploited to interpolate other useful quantities at the iso-surface, or anywhere within the cell.

A few implementations of the marching cubes algorithm are available in the open literature. However, they are limited to hexahedral grids. Thus, we developed a full 'marching cells' implementation that features the four possible cell types represented in Figure 4, where also their nodal and edge labeling conventions are reported: hexahedra, triangular prisms (or 'flatirons'), square pyramids and tetrahedra. The implementation is based on an object-oriented parameterized cell type that can be extended to further arbitrary cell types, and contains each cell type feature reported in Table 1.

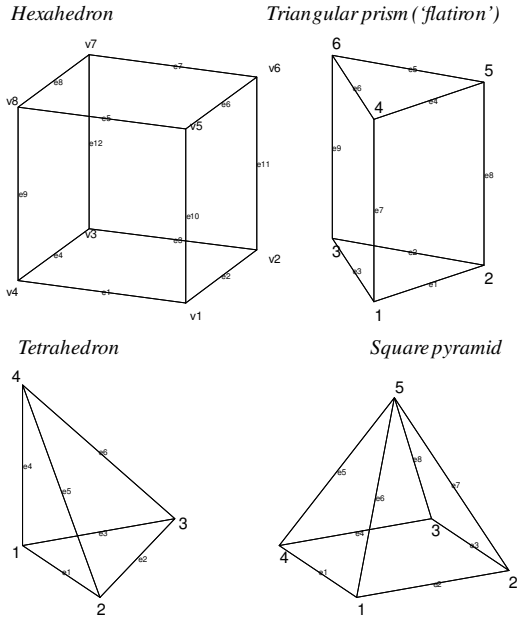

Figure 4. Cell types featured in the present study, and corresponding node and edge labeling conventions.

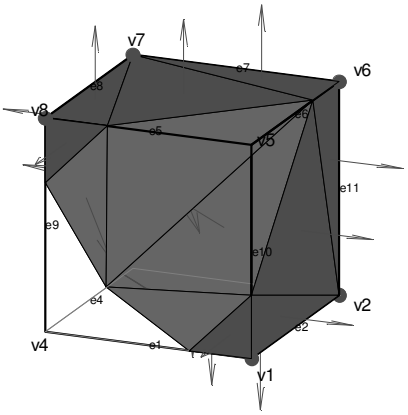

Figure 5. Iso-surface and volume triangulation of hexahedron configuration 231 (or 1110 0111): (blue) iso-surface triangles; (red) high-value region volume triangles, (dots) high-value nodes, (green) triangle normals.

Iso-surface case identification. In a typical iso-surface triangulation, a large number of cells is treated, leading to a possibly large number of triangles. Hence, for maximum computational speed, all possible iso-surface-in-cell configuration cases and corresponding triangle configurations were manually determined, and then stored in tables. A reference case setup is reported in Figure 5.

Each case is uniquely identified by its corresponding node configuration: by switching 'on' bits corresponding to nodes whose field value is greater than or equal to the iso-value (red dots in Figure 5), and 'off' bits corresponding to nodes whose field value is lower than the iso-value, one can build a binary string that points directly to a unique triangulation configuration in the global set of 2^n possible configurations, where n is the number of nodes in each cell.

For instance, in the configuration of Figure 5, the 8-bit string obtained by switching 'on' vertices 1, 2, 3, 6, 7 and 8 is 11100111, and corresponds to the integer value of 231, or a unique pointer to a row in the triangulation table, which features all possible configurations (0 to 255, in the case of a 8-node cell).

Triangulation mapping. The whole triangulation data space for all possible configurations of each different cell type was determined by manually mapping a subset of 'unique' iso-surface configurations, then extending it to the global configuration space exploiting symmetries (rotational and mirror-like).

Figure 6 reports the 23 unique configurations determined for a hexahedral cell: here, only rotational symmetry was exploited as it is acknowledged that mirror symmetry can lead to ambiguities in the internal triangle displacement [31]. 20 different triangulations were instead manually determined for a flatiron cell, as reported in Figure 7, from a total of 64 global; all 16 possible triangulations from a tetrahedron were instead directly mapped, as in Figure 8, and 12 unique configurations out of 32 total were instead mapped for a square pyramidal cell (Figure 9).

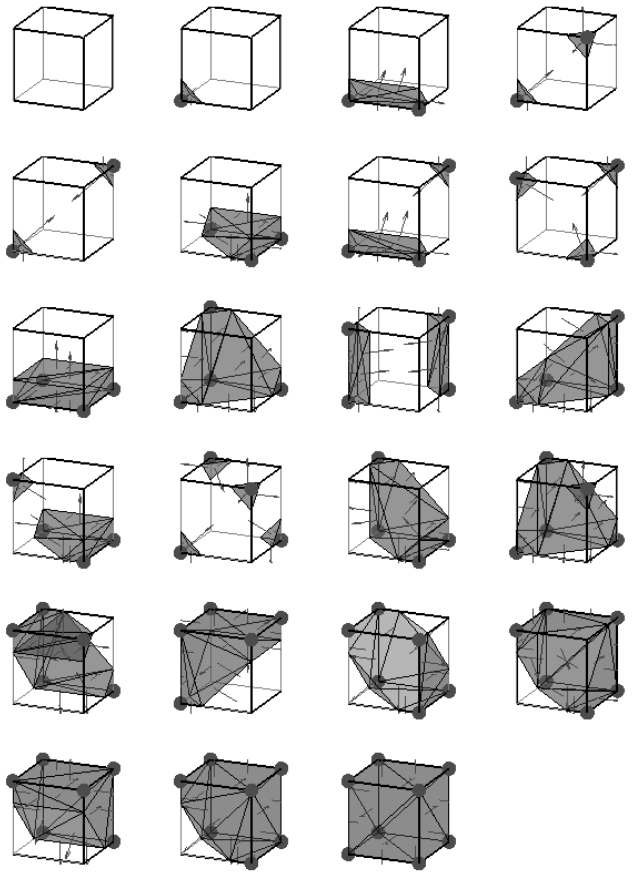

Figure 6. 23 unique iso-surface triangulations mapped for a hexahedral cell (256 total).

For each iso-surface configuration, the following pieces of information are mapped:

- number of iso-surface triangles;
- number of 'volumetric' triangles;
- map of iso-surface triangles: ordered list of edge indices, triangle normals pointing towards the low-value region;
- map of 'volumetric' triangles: ordered list of edge and node indices to build a complementary triangulation that encapsulates the high-value portion of the cell's volume; triangle normals pointing outwards of the encapsulated volume.

Iso-surface properties. The mapping tables were meant to contain all logical pieces of information to describe all geometric features of the iso-surface within the cell. The actual geometric displacement of the iso-surface needs to be determined from knowledge of the instantaneous nodal field values – hence, of the edge piercing point positions due to the multi-linear interpolation – and iso-value choice (which in the case of a G field is constant and equal to **G** = *0*). In particular, given a set of n_{iso} iso-surface triangles $(P_1P_2P_3)_i$, the total iso-surface area can simply be evaluated as:

$$A_{iso} = \sum_{i=1}^{n_{iso}} A_i = \frac{1}{2} \sum_{i=1}^{n_{iso}} \left| \left(P_{i,2} - P_{i,1} \right) \times \left(P_{i,3} - P_{i,1} \right) \right|. \qquad (15)$$

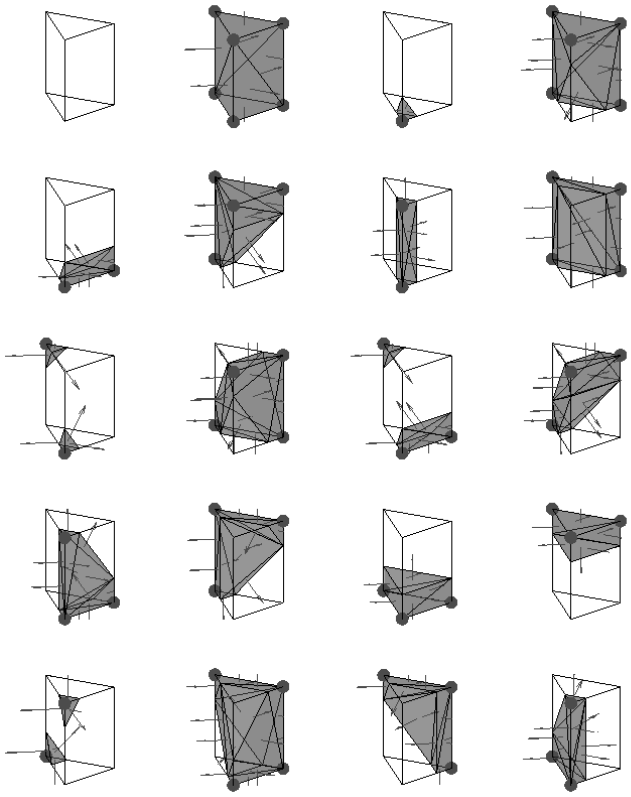

Figure 7. 20 unique iso-surface triangulations mapped for a triangular prism cell (64 total).

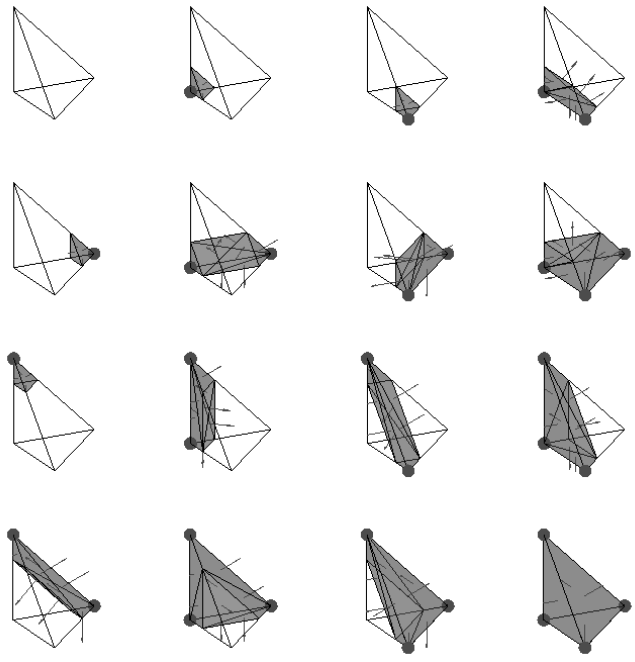

Figure 8. 16 iso-surface triangulations mapped for a tetrahedral cell (16 total).

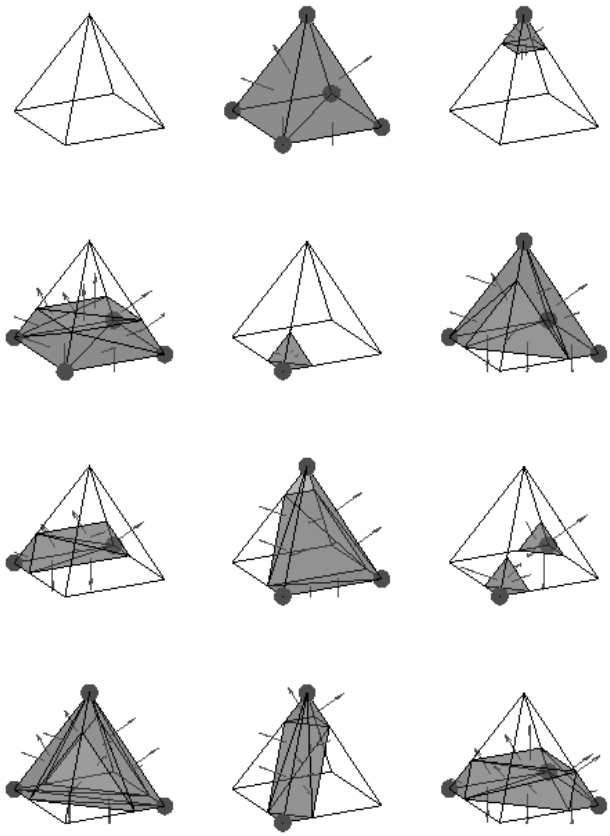

Figure 9. 12 unique iso-surface triangulations mapped for a pyramidal cell (32 total).

In the G-Equation model it is also crucial to know how much volume is being separated by the iso-surface into a low-value and a high-value region, that corresponds to a region of low-temperature unburnt mixture, and of high-temperature combustion products, that are treated as separated reactive systems for the computation of combustion kinetics.

As previously described as the definition of a 'volumetric' triangulation, complementary to each iso-surface triangulation, the volume of the high-value field region Ω which encloses the cell portion having field values greater than the chosen iso-value is defined as the three-dimensional integral over the region itself [32]:

$$V = \int_{\Omega} dV \; ; \tag{16}$$

by selecting a function in $\Re^3$ – such as the position function $\mathbf{x} = (x,y,z)$ – that has a constant divergence, one can turn the volume integral into a gradient integral:

$$\int_{\Omega} (\nabla \cdot \mathbf{x}) dV = \int_{\Omega} \left(\frac{\partial x}{\partial x} + \frac{\partial y}{\partial y} + \frac{\partial z}{\partial z} \right) dV = 3V \; , \tag{17}$$

and hence legally apply the divergence theorem:

$$V = \frac{1}{3}\int_{\Omega}(\nabla\cdot\mathbf{x})dV = \frac{1}{3}\oint_{\partial\Omega}\mathbf{x}\cdot\hat{n}\,dS$$
$$= \frac{1}{3}\sum_{i=1}^{n_{tri}}\oint_{\partial\Omega_i}\mathbf{x}\cdot\hat{n}\,dS = \frac{1}{3}\sum_{i=1}^{n_{tri}}\left(\oint_{\partial\Omega_i}\mathbf{x}\,dS\right)\cdot\hat{n}_i \qquad (18)$$
$$= \frac{1}{3}\sum_{i=1}^{n_{tri}}A_i\mathbf{x}_{G,i}\cdot\hat{n}_i,$$

where, in the case of a volume being wrapped by a triangulation made of n_{tri} triangles, $\mathbf{x}_{G,i}$ is (by definition) the barycenter of the i-th triangle enclosing the volume, A_i its area and n_i its outward-pointing normal vector.

In essence, both the iso-surface area and separated volumes are evaluated in a vectorizable and computationally efficient way by summing over a series of basic triangle-related computations, whose parameters are pre-tabulated at compilation level.

Spatial Discretization Scheme

A least-square gradient reconstruction scheme was implemented for the evaluation of the spatial derivatives describing the G field gradient and flame front curvature on general unstructured grids. In the approach of Tan and Reitz [14], an essentially non-oscillatory scheme was adopted [33], which featured the definition of a local Cartesian coordinate system for each cell and its first- and second-order neighbors to evaluate gradient and curvature terms.

However, since the definition of a local coordinate system in general unstructured meshes would require the definition of preferential directions (such as, for instance, in the quasi-second-order upwind fluxing procedure of KIVA4 [22]), a least-squares gradient reconstruction method was instead implemented [39], as 1) it does not require any *a-priori* field estimation, 2) the same implementation works for any generic unstructured nodal connectivity, 3) it isotropically achieves second-order spatial accuracy, and 4) it works at both the elemental node level and its execution can be vectorized at the finite-volume domain level.

According to this method, any mesh node *P* can be linked to an arbitrary number of neighbor nodes, as represented in Figure 10.

Assuming a finite difference representation of the gradient function between any pair of neighbor nodes, one has

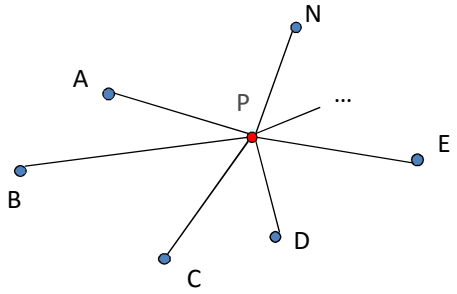

Figure 10. Generic nodal connectivity for a hybrid unstructured mesh.

$$(\nabla g)\cdot(\mathbf{x}_P - \mathbf{x}_A) = g_P - g_A,$$
$$\frac{\partial g}{\partial x}(x_P - x_A) + \frac{\partial g}{\partial y}(y_P - y_A) + \frac{\partial g}{\partial z}(z_P - z_A) = g_P - g_A, \qquad (19)$$

Hence, a linear equation with the gradient coefficients as unknowns can be written for each pair of neighbor nodes. Hence, per given node *P*, an over-determined linear system is written:

$$\begin{bmatrix} x_P - x_A & y_P - y_A & z_P - z_A \\ x_P - x_B & y_P - y_B & z_P - z_B \\ x_P - x_C & y_P - y_C & z_P - z_C \\ \cdots & \cdots & \cdots \\ x_P - x_N & y_P - y_N & z_P - z_N \end{bmatrix} \cdot \begin{bmatrix} \varphi_x \\ \varphi_y \\ \varphi_z \end{bmatrix} = \begin{bmatrix} g_P - g_A \\ g_P - g_B \\ g_P - g_C \\ \cdots \\ g_P - g_N \end{bmatrix} \qquad (20)$$

and its unknowns are solved for in a least-square sense using the QR decomposition of the nodal coordinate matrix.

The least-squares gradient reconstruction procedure was tested on a constant-volume cylindrical domain, discretized either with a hexahedral or with a tetrahedral mesh, where a normalized G field having a spherical $\boldsymbol{G} = 0$ iso-surface with 1cm diameter, as reported in Figure 11. The results show excellent consistency between the two meshes.

Finally, it is worth noting that this linear algebra was embedded in high-level code, such that the gradient and flame curvature calculations could be completed in few lines of code (Figure 12), allowing for future embedding of further spatial differentiation schemes.

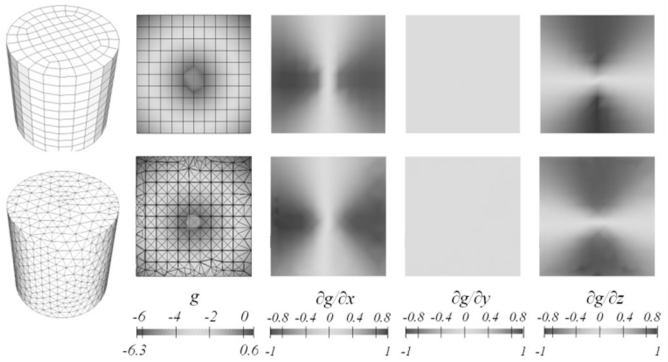

Figure 11. Gradient computation for a spherical G-field initialized with distance from the iso-value *g=0* around an ignition kernel. (top) hexahedral mesh, (bottom) tetrahedral mesh.

```
! Compute G field gradient
ggrad    = nabla(g(1:))

! Magnitude
ggradmag = norm2(ggrad,2)
rgradmag = merge(-one/ggradmag,zero,ggradmag>zero)

! Compute curvature km = div( -nabla(g)/|nabla(g)| )
kM = ddx(ggrad(:,1)*rgradmag,1)+ddx(ggrad(:,2)*rgradmag,2)+ddx(ggrad(:,3)*rgradmag,3)
```

Figure 12. Fortran 2008 [44] code for computing G field gradient and curvature.

Numerical Solution Procedure

The Favre-averaged G-Equation (4) was embedded in the KIVA-4 Arbitrary Lagrangian-Eulerian (ALE) solver framework [22], where the solution to any transport equation is essentially decoupled between a Lagrangian phase, where only source and diffusion terms are solved following a Lagrangian point of view, and an Eulerian phase, where advective transport is accounted for and the field quantities are fluxed from the Lagrangian node locations back to the Eulerian node locations. This approach has the advantage of allowing arbitrary movement of the mesh nodes during the simulation, which is particularly suitable for large volume changes such as those occurring in engines.

The G-Equation implementation was hence accordingly split between two phases.

0. G-Field initialization: once the kernel development is over, the G field is initialized based on the kernel particle locations: G = 0 at the particle locations; far away it is set to the signed distance from the particles.
1. During the Lagrangian phase, only the Lagrangian derivative is evaluated:

$$\begin{cases} \dfrac{\partial G}{\partial t} = \dfrac{\rho_u}{\rho} s_t^0 |\nabla G| - D_t k_M |\nabla G|, \\ k_M = \nabla \cdot \left(\dfrac{-\nabla G}{|\nabla G|} \right); \end{cases} \quad (21)$$

The computation is done in an explicit fashion, prior to the implicit pressure-velocity coupling calculation, similarly to what is done for plain chemical kinetics or any other ignition model.

2. Next, the G field values – now at Lagrangian locations – are fluxed back to the time n+1 Eulerian locations using the same quasi-second-order upwind scheme employed by KIVA-4 [22] for the momentum variables, subcycled in an explicit fashion according to a Courant constraint: the global time-step cannot exceed one Courant time-step, and each explicit sub-cycling step cannot exceed a fraction of the Courant step set to f_{con} = 0.2.
3. The G-field is re-normalized so that |∇G|=1 anywhere outside of the flame front [14].

Node-based computation. It should be noted that, in order to reduce the computational time and as the G-Equation has no meaning outside of the flame front, all the field computations actually only operate on the flame 'brush' region nodes.

As all the flame triangulation vertices happen to be on mesh edges, the list of edges pierced by the flame also defines a unique set of burnt vs. unburnt node pairs, as reported in Figure 13. Hence, the computation of the G-Equation source terms is computed by looping through the edges, consistently with the advection scheme later adopted by the CFD code [32]. The contributions of each edge are added to the node pair (i4b, i4u) and weighted by the node's Voronoi cell mass:

$$\begin{aligned} \left.\frac{\partial G}{\partial t}\right|_b &= \left.\frac{\partial G}{\partial t}\right|_b + m_b \left(\frac{\bar{\rho}_u}{\bar{\rho}_b} s_t^0 |\nabla G|_b - D_t \tilde{k}_{m,b} |\nabla G|_b \right) \\ \left.\frac{\partial G}{\partial t}\right|_u &= \left.\frac{\partial G}{\partial t}\right|_u + m_u \left(\frac{\bar{\rho}_u}{\bar{\rho}_b} s_t^0 |\nabla G|_u - D_t \tilde{k}_{m,u} |\nabla G|_u \right) \end{aligned}, \quad (22)$$

where the geometric terms |∇G| and k_m are already known at the node locations due to the least square reconstruction procedure, and cell-based quantities ρ, s_t, D_t are mass-averaged over the fully-burnt or fully-unburnt cell neighbors to the burnt and unburnt node, respectively.

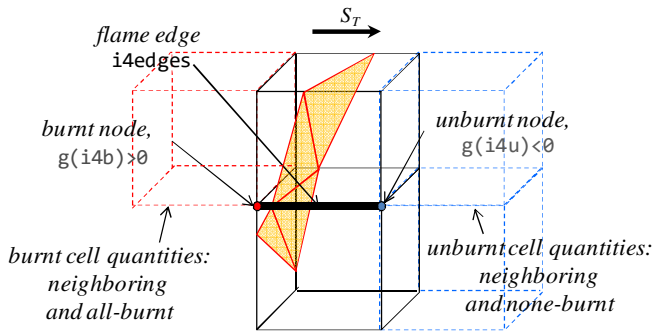

Figure 13. Schematic of the node-based G-Equation solution scheme.

The Voronoi mass-averaging assumption is instead based on the fact that, especially when the flame is wrinkled, each node can participate to more than one flame piercing edge.

Model Validation

Three different model validation test-cases were built in increasing order of complexity in order to assess the accuracy and consistency of the developed model to torch jet flame combustion across different mesh types. These cases feature ignition of gas-phase iso-octane, methane and propane mixtures at ambient pressures, whose laminar flame speeds were modeled using the relationships by Metghalchi and Keck [35]. The reaction mechanism by Ra and Reitz was used for the detailed chemical kinetics calculation [36]. This mechanism features 264 species and 1292 reactions, and was validated versus experimental measurements of ignition delay times, HCCI and spray engine combustion.

Constant-volume chamber with quiescent C_8H_{18}-air mixture

The model was first assessed in a constant-volume chamber simulation, featuring spark ignition of a stoichiometric iso-octane/air mixture at ambient pressure and initial temperature of 500K, as reported in Table 2. The chamber is cylindrically shaped, with 10 cm bore and height.

Table 2. Initial and boundary conditions for all validation test-cases.

	CVCC	Furukawa	Tasaka
Fuel	iC8H18	CH4	C3H8
ϕ	1.0	1.0	1.0
p_0 [bar]	1.0	1.0	1.5
T_0 [K]	500	550	340
Twall [K]	413.25	298.15	298.15
Initial turb. Intensity [%]	10.0	10.0	10.0
init. Δt [s]	5e-7	5e-7	5e-7
max Δt [s]	1e-5	1e-5	1e-2

Table 3. Cells and average edge length [cm] of each mesh used for the constant-volume chamber.

Cell Type	Mesh 1	Mesh 2	Mesh 3
Hexahedra	14,400 / 0.39	52,200 / 0.25	98,400 / 0.20
Tetrahedra	12,800 / 0.80	47,207 / 0.49	98,557 / 0.38
Pyramids	14,400 / 0.52	52,920 / 0.33	98,124 / 0.27
Flatirons	13,770 / 0.63	50,688 / 0.41	99,180 / 0.33

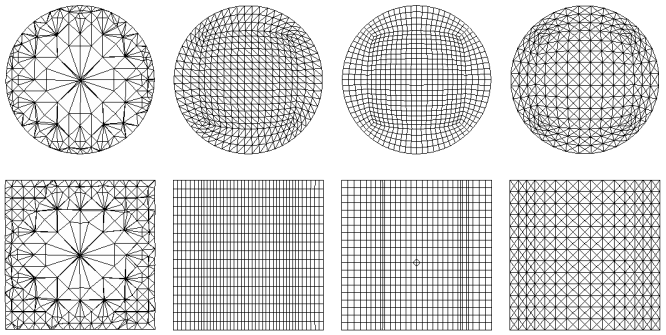

Fig. 14. Vertical and horizontal cross-sectional views of the constant volume chamber meshes (mesh type: 1, coarse) featuring different cell types. Left to right: tetrahedra, flatirons, hexahedra, pyramids.

Four different mesh types were generated, each featuring a different cell type: Hexahedra, Tetrahedra, Pyramids and Flatirons. Then, for each cell type, three different meshes were generated having different resolutions. Consistency among the different types was kept by using similar numbers of cells in each mesh class, as reported in Table 3.

Figure 14 also reports cross-sectional views of the four mesh types used: the pyramidal and prismatic (flatirons) meshes are both derived from the same o-grid scheme as the hexahedral mesh, by splitting the hexahedra either in two or in 6 child cells. The tetrahedral mesh is instead automatically generated from an octree-based triangulation with wall refinement.

A comparison of predicted flame propagation histories for the coarsest and most refined mesh types (type 1 and 3, respectively) is reported in Figure 15: all four mesh types show pretty similar timings and a common near-spherical flame development, which stretches up to the liner, and then disappears as the flame sweeps progressively more unburnt volume. Consistent behavior was seen also across the mesh resolutions, per each cell type: a more refined mesh always leads to an earlier flame propagation. Also, at comparatively similar resolutions, the tetrahedral meshes appear to underestimate flame propagation in comparison with all other three mesh types, which instead exhibit similar behavior. This suggests that tetrahedral meshes - that feature a low number of nodes per number of cells ratio in comparison with the other cell types - can suffer some under-resolution issues of the G-Equation model in comparison with the other fields, as in the KIVA-4 staggered grid approach the G field, similarly as the velocity field, is stored at the node positions instead of at the cell centroids.

As also reported in Figure 16 in terms of time histories of the global flame surface area, all mesh types show an advancement of predicted flame propagation when a more refined mesh resolution is used. This behavior appears converged for pyramidal and hexahedral cell types, while some form of grid dependency is still present in both flatiron and tetrahedral cells, even when the highest resolution is used.

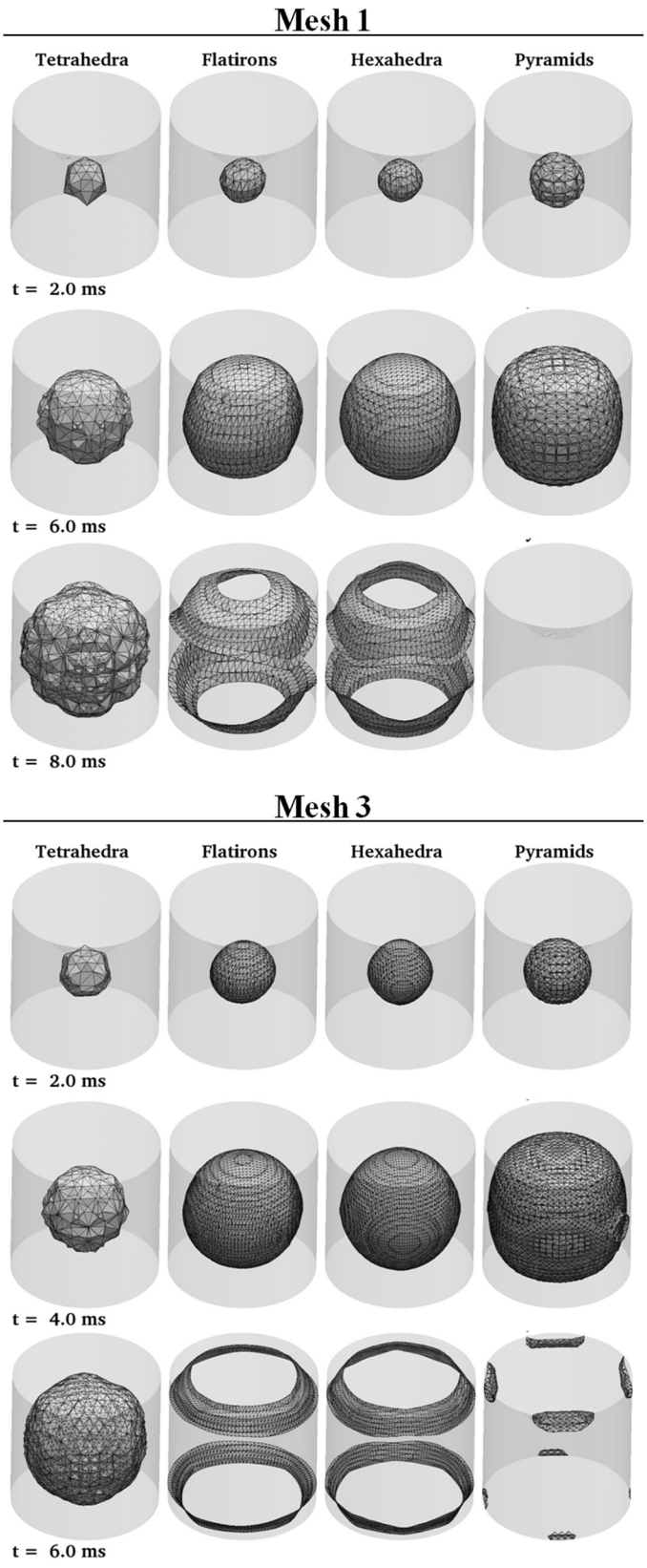

Fig. 15. Dependency of flame surface triangulations on cell type for (top) Mesh type 1 – coarse; (bottom) Mesh type 3 – refined.

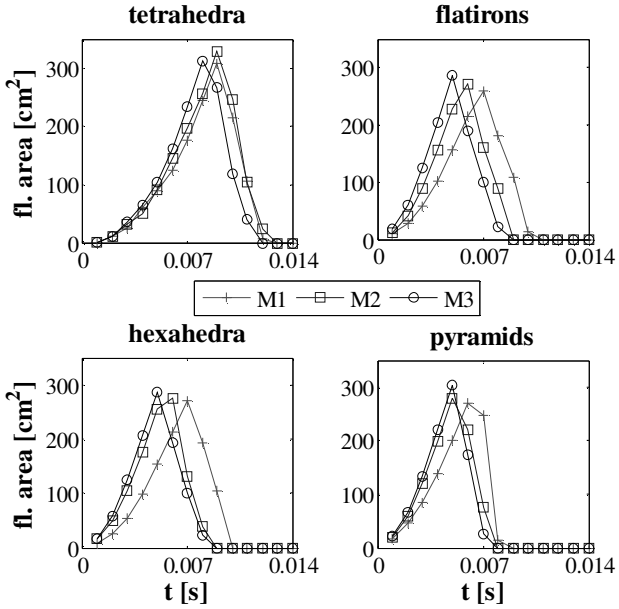

Fig. 16. Dependency of predicted time histories of flame surface area on cell types (different plots) and mesh types (different line colors).

Torch jet flame chamber with diaphragm restriction

Furukawa's experiment [37] was used as the first test case for torch jet ignition of a gaseous fuel. In the experiment, a cylindrical diaphragm was placed in a rectangular optically-accessible chamber (as modeled in Figure 17), to create two separate regions. A stoichiometric air-methane mixture was ignited in the smaller pre-chamber, and the flame propagation through the diaphragm and the corresponding torch flame development into the main chamber were visualized using Schlieren imaging.

Three different orifice sizes of 8, 10 and 15 mm were tested in the experiments, and accordingly reproduced in the simulations. All meshes, as reported for the 8 mm orifice case in Figure 8 were made purely tetrahedral, with local refinement at the diaphragm. The mesh cell size parameters are reported in Table 4.

Figures 18,19,20 report predicted flame penetration into the secondary chamber versus experimental Schlieren imaging with each orifice diameter. The three different orifice diameters lead to different maxmum velocities, which give the flame a different penetration and structure. In the D=8 mm case (Figure 18), the tiny orifice size leads to large accelerations, and a 'mushroom'-like shape to the flame in the main chamber.

Table 4. Furukawa's chamber mesh rules used for each orifice geometry.

Mesh Type	Avg. size [cm]	Min. size [cm]
1	0.25	0.05
2	0.35	0.075
3	0.50	0.1

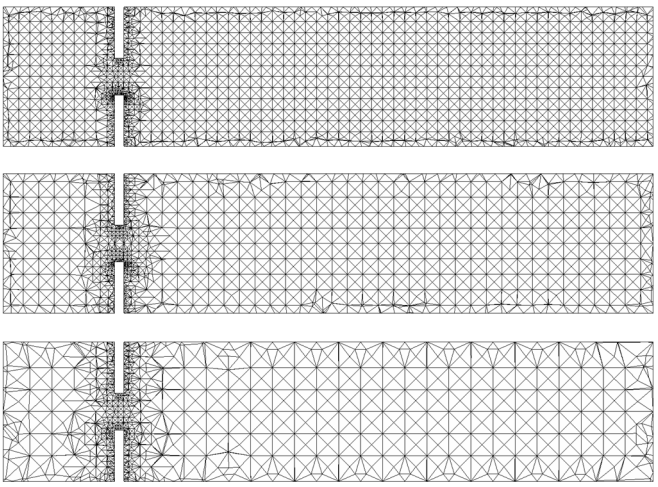

Fig. 17. Cross-sectional view of three domain discretizations for Furukawa's experiment, *d = 8 mm*.

At these conditions, the coarsest mesh size is not able to capture the smallest wrinkles, as well as the penetration, which is retarded. The more refined meshes show increased predicted penetration with increased resolution, which ultimately leads to a good agreement with the experiment, when the flame front has fully developed within the main chamber. However, the mesh coarsening downstream of the orifice is still responsible for a slightly inaccurate prediction of the transient flame jet shape at t = 2.0 ms even with the most refined mesh. The jet appears to be over-diffused downstream of the orifice, and the correct flame shape is lost.

In the D = 10 mm and D = 15 mm cases (Figures 19,20), all meshes show similar flame penetration, even if – again – only mesh types 1 and 2 are able to correctly represent both penetration and flame shape. Interestingly, only mesh 1 is able to capture the 'mushroom' shape wrinkles extending back towards the orifice plate edge, as the flame occupies the main chamber volume at t=2.0 ms. Overall, the flame propagation model appears to correctly capture flame structure and penetration if an appropriate mesh resolution is used.

Torch jet combustion with pre-chamber ignition

The experimental measurements of Tasaka *et al.* [38] feature a more realistic pre-chamber ignition case. The experimental apparatus, whose cross-sectional modeling is reported in Figure 21, features an upper cylindrical pre-chamber physically distant from a lower rectangular chamber, connected through a nozzle. Various nozzle sizes were tested in the experiments, where a slightly boosted (1.5 bar, Table 2) stoichiometric propane-air mixture was ignited through a spark plug located approximately halfway in the pre-chamber.

Table 5. Tasaka's chamber mesh data used for each nozzle diameter.

Mesh Type	Avg. size [cm]	Min. size [cm]
1	0.50	0.025
2	0.70	0.035
3	1.00	0.050

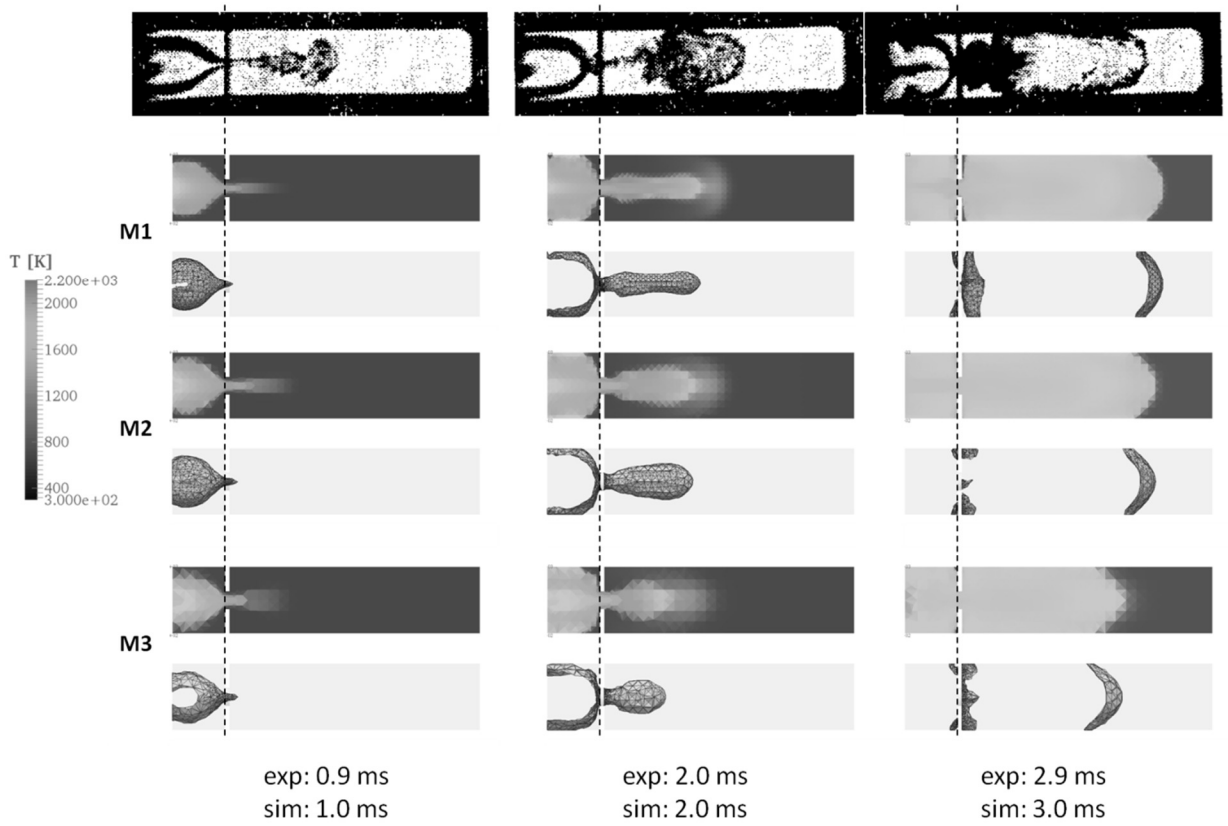

Figure 18. Predicted temperature profiles and flame triangulation vs. experimental Schlieren imaging, orifice D=8 mm [37].

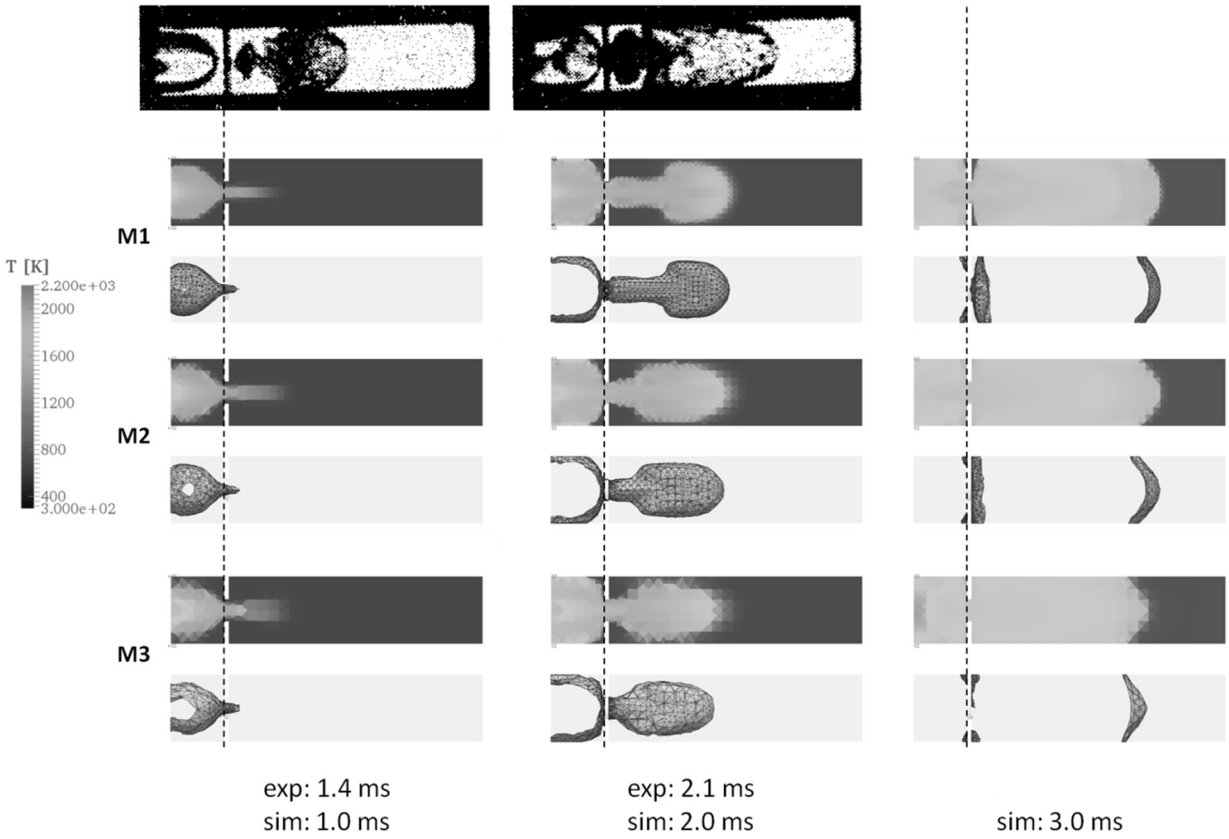

Figure 19. Predicted temperature profiles and flame triangulation vs. experimental Schlieren imaging, orifice D=10 mm [37].

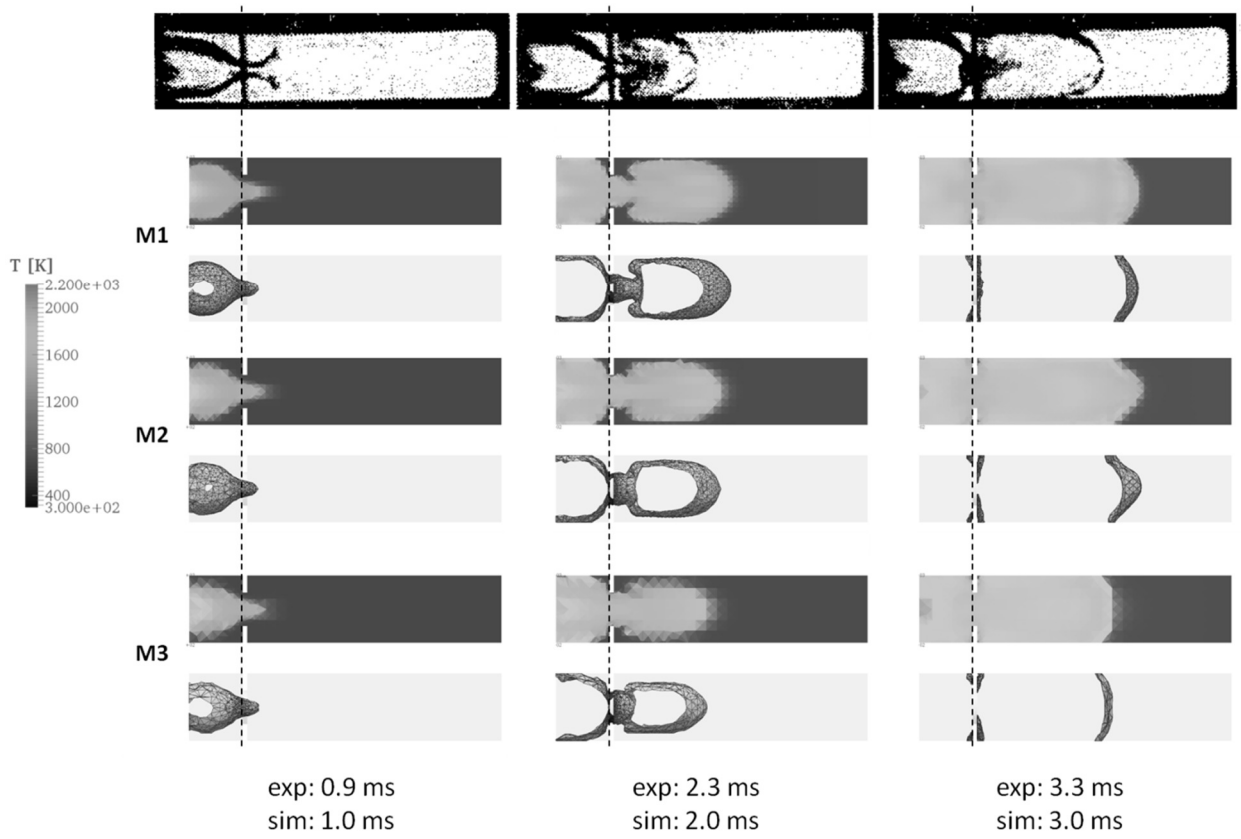

Figure 20. Predicted temperature profiles and flame triangulation vs. experimental Schlieren imaging, orifice D=15 mm [37].

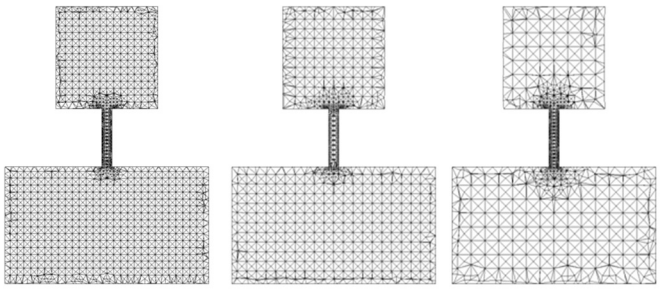

Fig. 21. Cross-sectional view of three domain discretizations for Tasaka's experiment, *d = 7 mm*.

Similarly to the approach adopted for the orifice restriction experiment, three meshes were generated, having different progressively-increasing resolutions both in the bulk and near-wall regions, as reported in Table 5 and Figure 21. Some uncertainties were present in setting initial and boundary conditions, as initial mixture temperature as well as spark plug location and electrode geometry were not reported. An initial temperature of 334 K was assumed as result of a hypothesized polytrophic compression of the mixture from ambient conditions.

Tasaka's experiments featured three different nozzle sizes of d=7, 10, 14 mm. Figure 22 reports a comparison between predicted and measured torch jet development and penetration into the main chamber using the smallest nozzle size. *d=7mm* is the most challenging case from a computational standpoint because of the higher, nearer-to-sonic velocities within the nozzle, and the smaller mesh resolution required to accurately capture the flame transport within the nozzle.

However, despite some timing discrepancies that can be related back to the uncertainties in initial conditions and spark plug location, geometry, energizing time, the amount of time (~4 ms) needed by the torch jet to travel through the nozzle and reach the main chamber wall was well predicted. Also the torch jet structure was in line with the shape shown by the Schlieren imaging, including the vortex formation after hitting against the wall, and backward chamber bulk combustion. Finally, the effects of varying nozzle shape appeared well captured by the simulations in terms of both penetration and torch jet angle trends, as reported in Figure 23: the jet angle dependency on nozzle diameter is seen to lead to a wider jet angle and a more spread flame propagation into the main chamber, as reported by the Schlieren imaging.

Concluding Remarks

In this work a computational model of flame propagation suitable for the simulation of natural-gas ignition in heavy-duty engine pre-chambers was developed and implemented using the ALE RANS CFD framework KIVA [22]. The computational

model features solution of the G-Equation for premixed or partially-premixed flames on hybrid unstructured grids, and uses detailed chemical kinetics for the computation of the rates of mass change of the species in the

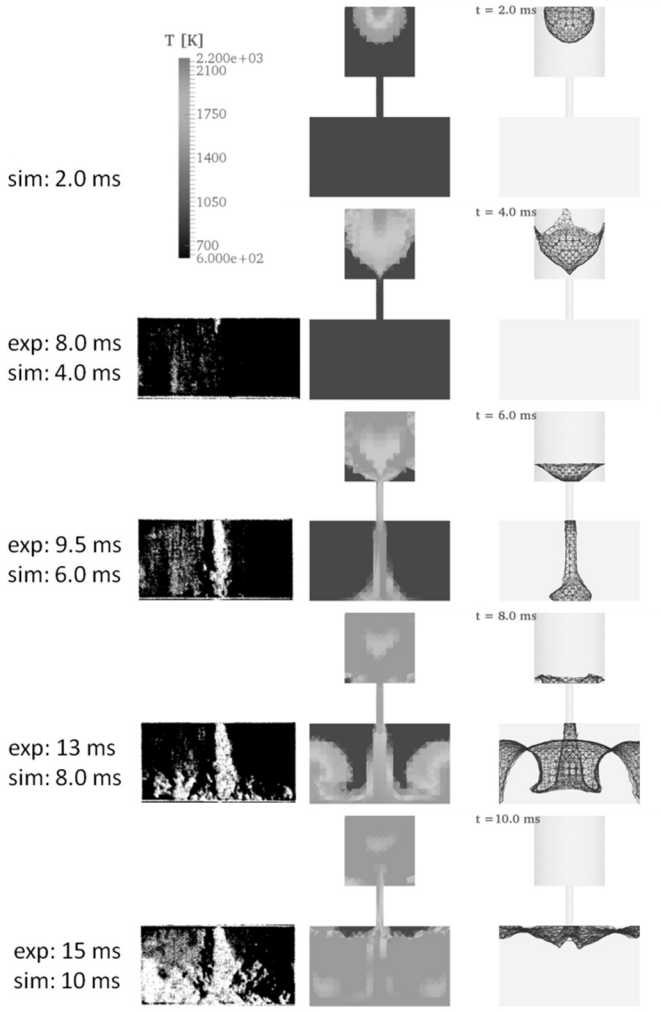

Figure 22. Comparison between predicted (mesh type 2) and measured (from [38]) torch jet penetration for Tasaka's experiment, *d=7 mm*

domain swept by the flame surface, while equilibrium is assumed at the flame's inner layer. Validation was carried out versus experiments relevant to pre-chamber ignition, which feature ignition in constant-volume chambers and torch-jet formation after a restriction (a diaphragm or a nozzle). The following conclusions were reached:

- The second-order spatial accuracy achieved with the least-squares gradient reconstruction method and QSOU advection scheme for the level set provided adequate predicted flame front shape and penetration, suggesting for the acceptability of the proposed node-based G-field discretization scheme.

- Tetrahedral meshes were seen to be slightly less accurate than hexahedron-derived meshes at similar number of cells, because of the significantly lower node-to-cell ratio, which leads to reduced G field resolution. However, they take advance of automatic mesh generation flexibility, which eases CFD testing of different pre-chamber geometries.

- Flame front penetration into the main chamber was well predicted for all mesh resolutions, and was only partially affected by mesh resolution. The greatest penalty of using the coarsest meshes was the (intrinsic) inability to capture small-

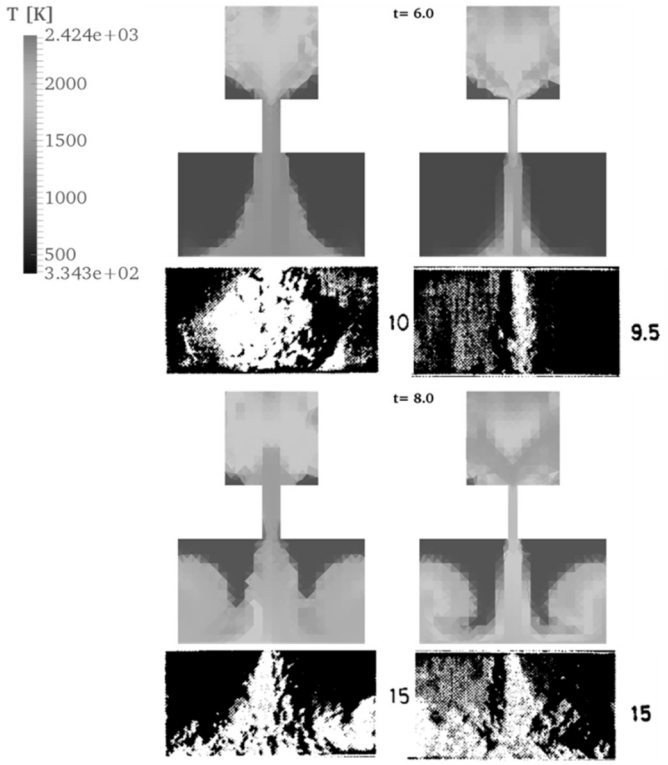

Figure 23. Comparison between predicted (mesh type 2) and measured [38] torch jet flame shapes in the main chamber with a nozzle diameter *d=14 mm* (left) or *d=7 mm* (right).

scale flame wrinkles. This again conveys robustness of the proposed spatial discretization scheme.
- The proposed flame tracking model has the potential for a wide range of applicability thanks to the usage of direct chemical kinetics calculations, that ensure much greater accuracy than tabulated or fitted-single-equation models. Future research will focus on improving laminar flame speed predictions by introducing a locally one-dimensional reaction-diffusion flame equation.

These results suggest that the present method can be successfully adopted for the design of heavy-duty gas-fueled spark ignition engines with pre-chambers.

References

1. Reitz RD, "Directions in internal combustion engine research", Comb Flame 160(1), 1-8, 2013.
2. Rutland CJ, "Large-eddy simulations for internal combustion

engines – a review", International Journal of Engine Research 2011, 12(5), 421-451. Doi: 10.1177/1468087411407248.
3. Wang B-L, Lee C-W, Reitz RD, Miles PC, Han Z., "A Generalized RNG turbulence model and its application to a light-duty diesel engine operating in a low temperature combustion regime," International Journal of Engine Research 14(3), 279-292, 2013.
4. Perini F, Miles PC, Reitz RD, "A comprehensive modeling study of in-cylinder fluid flows in a high-swirl, light-duty optical diesel engine," Computers and Fluids 105, 113-124, 2014. Doi:10.1016/j.compfluid.2014.09.011.
5. Perini F, Galligani E, Reitz RD, "An analytical Jacobian approach to sparse reaction kinetics for computationally efficient combustion modelling with large reaction mechanisms," Energy and Fuels, 26 (8), 4804-4822, 2012. Doi: 10.1021/ef300747n.
6. Perini F, Galligani E, Reitz RD, "A study of direct and Krylov iterative sparse solver techniques to approach linear scaling of the integration of Chemical Kinetics with detailed combustion mechanisms," Combustion and Flame 161(5) 1180-1195, 2014.
7. Liang L and Reitz RD, "Spark Ignition Engine Combustion Modeling Using a Level Set Method with Detailed Chemistry," SAE Technical Paper 2006-01-0243, 2006, doi:10.4271/2006-01-0243.
8. Liang L, Reitz RD, Iyer C, and Yi J, "Modeling Knock in Spark-Ignition Engines Using a G-equation Combustion Model Incorporating Detailed Chemical Kinetics," SAE Technical Paper 2007-01-0165, 2007, doi:10.4271/2007-01-0165.
9. Ra Y, Kong S, Reitz RD, Rutland CJ et al., "Multidimensional Modeling of Transient Gas Jet Injection Using Coarse Computational Grids," SAE Technical Paper 2005-01-0208, 2005, doi:10.4271/2005-01-0208.
10. Abani N and Reitz RD, "Unsteady turbulent round jets and vortex motion", Physics of Fluids 19, 125102, 2007. doi: 10.1063/1.2821910.
11. Perini F and Reitz RD, "Improved atomization, collision and sub-grid scale momentum coupling models for transient vaporizing engine sprays", International Journal of Multiphase Flow, 79, 107-123, 2016. doi:10.1016/j.ijmiltuphaseflow.2015.10.009.
12. Peters N, "Turbulent Combustion", Cambridge University Press, 2000.
13. Peters N, "The Turbulent Burning Velocity for Large Scale and Small Scale Turbulence", Journal of Fluid Mechanics 384, 107-132, 1999.
14. Tan Z and Reitz RD, "Modeling Ignition and Combustion in Spark-ignition Engines Using a Level Set Method", SAE Technical paper 2003-01-0722, 2003.
15. Poinsot TJ, Haworth DC, Cruneaux G, "Direct Simulation and Modeling of Flame-Wall Interaction for Premixed Turbulent Combustion", Combustion and Flame 95, 1993:118-132.
16. Nieman D, Dempsey A, Reitz RD, "Heavy-Duty RCCI Operation Using Natural Gas and Diesel," SAE Int. J. Engines 5(2):270-285, 2012, doi:10.4271/2012-01-0379.
17. Wall J, Heywood J, "The Influence of Operating Variables and Prechamber Size on Combustion in a Prechamber Stratified-Charge Engine," SAE Technical Paper 780966, 1978, doi:10.4271/780966.
18. Ryu H, Asanuma T, "Numerical Simulation of Two-Dimensional Combustion Process in a Spark Ignition Engine with a Prechamber using k - ε Turbulence Model," SAE Technical Paper 890669, 1989, doi:10.4271/890669.
19. Toulson E, Schock H, Attard W, "A Review of Pre-Chamber Initiated Jet Ignition Combustion Systems," SAE Technical Paper 2010-01-2263, 2010, doi:10.4271/2010-01-2263.
20. Shah A, Tunestal P, Johansson B, "Investigation of Performance and Emission Characteristics of a Heavy Duty Natural Gas Engine Operated with Pre-Chamber Spark Plug and Dilution with Excess Air and EGR," SAE Int. J. Engines 5(4):1790-1801, 2012, doi:10.4271/2012-01-1980.
21. Shah A, Tunestal P, Johansson B, "Effect of Pre-Chamber Volume and Nozzle Diameter on Pre-Chamber Ignition in Heavy Duty Natural Gas Engines, " SAE Technical Paper 2015-01-0867, 2015, doi:10.4271/2015-01-0867.
22. Torres DJ, Trujillo MF, "KIVA-4: An unstructured ALE code for compressible gas flow with sprays", Journal of Computational Physics 219, 2006:943-975.
23. Peters N, "Laminar Flamelet Concepts in Turbulent Combustion", Proceedings of the 25th Symposium (International) on Combustion, 1986, 1231-1250.
24. Osher S, Fedkiw R, "Level Set Methods and Dynamic Implicit Surfaces", Springer-Verlag, 2002, ISBN 978-0-387-22746-7.
25. Fan L and Reitz RD, "Development of an Ignition and Combustion Model for Spark-Ignition Engines," SAE Technical Paper 2000-01-2809, 2000, doi:10.4271/2000-01-2809.
26. Herweg R, Maly RR, "A Fundamental Model for Flame Kernel Formation in SI Engines", SAE Technical Paper 922243, 1992. doi: 10.4271/922243.
27. Pope SB, "Gibbs function continuation for the stable computation of chemical equilibrium", Combustion and Flame 139(3), 222-226, 2004.
28. Lorensen WE, Cline HE, "Marching cubes: a high resolution 3D surface construction algorithm", ACM SIGGRAPH '87 Proceedings of the 14th annual conference on Computer graphics and interactive techniques, 163-169, 1987, doi: 10.1145/37402.37422
29. Nielson GM, "On Marching Cubes", IEEE Transactions on Visualization and Computer Graphics 9(3), 2003:283-297.
30. Newman TS, "A survey of the Marching Cubes Algorithm", Computers & Graphics 30 (2006), 854-879.
31. Banks DC, Linton S, "Counting Cases in Marching Cubes: Toward a Generic Algorithm for Producing Substitopes", IEEE Visualization 2003, October 19-24, 2003, Seattle (WA), USA.
32. Wang S, "3D Volume Calculation For the Marching Cubes Algorithm in Cartesian Coordinates", arXiv:1308.0387v1 [math.NA], 2013.
33. Harten A, Engquist B, Osher S, Chakravarthy S, "Uniformly High-Order Accurate Essentially Non-oscillatory schemes III", J. Comp. Phys 71(2), 1987:231-303.
34. Reid J, "The new features of Fortran 2008", ACM SIGPLAN Fortran Forum 27(2), 2008:8-21. doi: 10.1145/1408643.1408645.
35. Metghalchi M and Keck JC, "Burning Velocities of Mixtures of Air with Methanol, Isooctane, and Indolene at High Pressure and Temperature", Combustion and Flame 48, 1982:191-210.
36. Ra Y, and Reitz RD, "A combustion model for multi-component fuels using a physical surrogate group

chemistry representation (PSGCR)," Combustion and Flame, doi: 10.1016/j.combustflame.2015.05.014, 2015.
37. Furukawa J, Gomi T, “Propagation of Turbulent Flame-Jet in a Closed Vessel”, JSME Series B, Vol. 47, No. 414, 1982.
38. Tasaka H, Mikogami T, Matsuoka S, “Heat Loss and Heat Release on Premixed Combustion in a Divided Chamber Combustion Bomb”, JSME Series B, Vol. 50, No. 454, 1984.
39. Mavriplis DJ, “Revisiting the Least-Squares Procedure for Gradient Reconstruction on Unstructured Meshes”, 16th AIAA Computational Fluid Dynamics Conference, AIAA 2003-3986, 2003.

Contact Information

Federico Perini
Engine Research Center
University of Wisconsin-Madison
1015A Engineering Research Building
1500 Engineering Drive
Madison, WI 53706 (USA)
perini@wisc.edu

Acknowledgments

The authors wish to acknowledge support for this research by Mitsubishi Heavy Industries, Ltd. ANSYS Inc. is gratefully acknowledged for providing licenses of the ICEM CFD meshing tool.

Definitions/Abbreviations

ALE	Arbitrary Lagrangian-Eulerian
aTDC	After Top Dead Center
CFD	Computational Fluid Dynamics
cfg	Configuration
DPIK	Discrete Particle Ignition Kernel
ENO	Essentially Non-Oscillatory
LES	Large-Eddy simulation
ODE	Ordinary Differential Equations
QSOU	Quasi-second-order Upwind
RANS	Reynolds-Averaged Navier-Stokes
UHC	Unburnt Hydrocarbons